HAL
open science

Intraband absorption in self-assembled Ge-doped GaN/AlN nanowire heterostructures

M. Beeler, P. Hille, J. Schörmann, J. Teubert, M. de la Mata, J. Arbiol, M. Eickhoff, E. Monroy

To cite this version:

M. Beeler, P. Hille, J. Schörmann, J. Teubert, M. de la Mata, et al.. Intraband absorption in self-assembled Ge-doped GaN/AlN nanowire heterostructures. Nano Letters, 2014, 14 (3), pp.1665-1673. 10.1021/nl5002247 . hal-02119215

HAL Id: hal-02119215

https://hal.science/hal-02119215v1

Submitted on 10 Feb 2024

HAL is a multi-disciplinary open access archive for the deposit and dissemination of scientific research documents, whether they are published or not. The documents may come from teaching and research institutions in France or abroad, or from public or private research centers.

L'archive ouverte pluridisciplinaire **HAL**, est destinée au dépôt et à la diffusion de documents scientifiques de niveau recherche, publiés ou non, émanant des établissements d'enseignement et de recherche français ou étrangers, des laboratoires publics ou privés.

NANO LETTERS

Letter

pubs.acs.org/NanoLett

Intraband Absorption in Self-Assembled Ge-Doped GaN/AlN Nanowire Heterostructures

M. Beeler,[†] P. Hille,[‡] J. Schörmann,[‡] J. Teubert,[‡] M. de la Mata,[§] J. Arbiol,[§,∥] M. Eickhoff,[‡] and E. Monroy*,[†]

[†]CEA-CNRS Group Nanophysics and Semiconductors, CEA/INAC/SP2M and CNRS-Institute Néel, 17 rue des Martyrs, 38054 Grenoble cedex 9, France

[‡]I. Physikalisches Institut, Justus-Liebig-Universität Gießen, Heinrich-Buff-Ring 16, D-35392 Gießen, Germany

[§]Institut de Ciencia de Materials de Barcelona, ICMAB-CSIC, Campus de la UAB, 08193 Barcelona, Catalonia, Spain

[∥]Institucio Catalana de Recerca i Estudis Avançats (ICREA), 08010 Barcelona, Catalonia, Spain

Downloaded via CEA SACLAY on February 10, 2024 at 10:16:39 (UTC).
See https://pubs.acs.org/sharingguidelines for options on how to legitimately share published articles.

ABSTRACT: We report the observation of transverse-magnetic-polarized infrared absorption assigned to the s−p_z intraband transition in Ge-doped GaN/AlN nanodisks (NDs) in self-assembled GaN nanowires (NWs). The s−p_z absorption line experiences a blue shift with increasing ND Ge concentration and a red shift with increasing ND thickness. The experimental results in terms of interband and intraband spectroscopy are compared to theoretical calculations of the band diagram and electronic structure of GaN/AlN heterostructured NWs, accounting for their three-dimensional strain distribution and the presence of surface states. From the theoretical analysis, we conclude that the formation of an AlN shell during the heterostructure growth applies a uniaxial compressive strain which blue shifts the interband optical transitions but has little influence on the intraband transitions. The presence of surface states with density levels expected for *m*-GaN plane charge-deplete the base of the NWs but is insufficient to screen the polarization-induced internal electric field in the heterostructures. Simulations show that the free-carrier screening of the polarization-induced internal electric field in the NDs is critical to predicting the photoluminescence behavior. The intraband transitions, on the other hand, are blue-shifted due to many-body effects, namely, the exchange interaction and depolarization shift, which exceed the red shift induced by carrier screening.

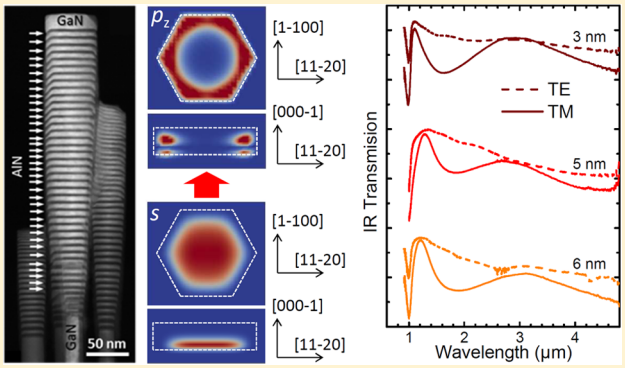

KEYWORDS: *Nanowire, GaN, intraband, intersubband*

As optoelectronic devices push toward higher efficiencies, the control of carrier relaxation becomes a key aspect for device engineering, which is particularly relevant in the case of intraband/intersubband (ISB) optoelectronics (quantum well infrared photodetectors, quantum cascade detectors, quantum cascade lasers). Longer intraband lifetimes have been proven to exist in laterally confined systems, including quantum dots (QDs)[1−4] and nanowires (NWs).[5,6] In the case of NWs, their large surface-to-volume ratio allows misfit strain to be elastically released, extending the viable active region size and composition beyond the limits of planar systems or QDs. For these reasons, NWs are under study to improve the performance of THz quantum cascade lasers,[7,8] whose operating temperature is currently limited by nonradiative scattering processes which quickly depopulate the upper laser level.

Semiconductor NWs have already become a powerful kind of nanomaterial with promising applications in electronics,[9] optoelectronics,[10,11] energy conversion,[12,13] and sensorics.[14,15] However, not much information has been reported so far on NW intraband electronic transitions. From the experimental viewpoint, infrared (IR) optical absorption associated to intraband transitions between laterally confined states have been observed in bismuth NWs,[16] and intraband effects have proven relevant to understand the operation of Si-NW field effect transistors.[17] However, conduction band fluctuations associated to stacking faults and polytypism[18−20] have hindered the realization of intraband optoelectronic devices using self-assembled GaAs-based heterostructured NWs (bottom-up approach). As an alternative, intraband electroluminescence was recently obtained from nanopilars lithographically defined on a standard GaAs/AlGaAs quantum cascade laser structure (top-down approach).[21]

GaN could be a model material for the study of intraband transitions in heterostructured NWs, since the presence of

Received: January 20, 2014
Published: February 6, 2014

 © 2014 American Chemical Society dx.doi.org/10.1021/nl5002247 | *Nano Lett.* 2014, 14, 1665−1673

stacking faults or extended defects can be limited to the first hundred nanometers close to the substrate. III-nitrides have recently emerged as promising semiconductors for new intraband devices.[22−24] GaN is transparent over a large spectral region, notably for wavelengths longer than 360 nm, reaching into the far-IR, excluding the Restrahlen band (from 9.6 to 19 μm). Additionally, the large energy of GaN's longitudinal-optical (LO) phonons (92 meV) opens prospects for high-temperature THz quantum cascade lasers and intraband devices covering the 5−10 THz band, inaccessible to As-based technologies due to phonon absorption. Furthermore, their large conduction band offset (about 1.8 eV for GaN/AlN[25−27]) and subpicosecond intraband relaxation times[28−31] render them appealing materials for ultrafast photonic devices from the near to the far-IR.[32,33] Currently, ISB absorption in GaN/AlGaN quantum wells (QWs) can be tuned from 1.0 to 10 μm,[34−39] and in the THz range (>20 μm).[40−42] Room-temperature transverse-magnetic (TM) polarized near-IR intraband absorption in GaN/AlN QDs has also been reported.[1−4] This absorption was attributed to transitions from the ground state of the conduction band, *s*, to the first excited electronic state confined along the growth axis, p_z. The lateral confinement in the QDs gives rise to additional transitions that react to transverse-electric (TE) polarized excitation. The optical signature associated to s−$p_{x,y}$ was observed in the mid-IR by Vardi et al.[4] using in-plane electronic transport at low temperatures. However, shifting the s−p_z transition toward the mid- or far-IR is hindered by the requirement of lattice mismatch for the QD formation following the Stranski−Krastanov growth mode. Regarding GaN NWs, the only experimental result has been reported by Tanaka et al.,[43] who observed polarization-dependent near-IR absorption in a sample containing GaN/AlN (1 nm/2.7 nm) NW heterostructures. Furthermore, the feasibility of electron transport via quantized levels in the conduction band of GaN/AlN heterostructured NWs was demonstrated by the fabrication of resonant tunneling diodes.[32,33]

In this Letter, we first present a theoretical study of the intraconduction-band electronic structure of GaN/AlN heterostructured NWs, accounting for the strain distribution and the presence of surface states. Then, we report the experimental observation of TM-polarized IR absorption assigned to the s−p_z intraband transition in Ge-doped GaN/AlN nanodisks (NDs) inserted in self-assembled GaN NWs grown on Si(111) by plasma-assisted molecular-beam epitaxy (PAMBE). The s−p_z absorption line experiences a blue shift with increasing ND-doping level and a red shift with increasing ND thickness. The experimental results in terms of interband and intraband spectroscopy are compared with the theoretical calculations, and the inclusion of many-body effects is found to be critical in estimating the electronic transitions. Carrier screening of the polarization-induced internal electric field is critical for understanding the photoluminescence (PL) behavior of the NDs, and the intraband transitions are blue-shifted from the exchange interaction and depolarization shift, which overpower the red shift induced by carrier screening.

Theoretical Calculations. Three-dimensional (3D) calculations of the NW strain state, band diagram, and quantum confined states were performed using the Nextnano3 Schrödinger-Poisson equation solver.[44] The parameters used for GaN and AlN calculations are summarized in a previous paper.[45] We assumed a residual *n*-type doping $N_D = 5 \times 10^{17}$ cm^{-3}, and the dopant concentration in the GaN NDs was $N_D = 5 \times 10^{19}$ cm^{-3}. The NW was defined as a hexagonal prism consisting of a long (50 nm) GaN section followed by a sequence of 14 AlN/GaN stacks and capped with 18 nm of GaN. The growth axis was [000−1].[46,47] The NW GaN base radius was simulated to be 20 nm. The structure was defined on a GaN substrate, to provide a reference in-plane lattice parameter. The NW GaN base and the AlN/GaN heterostructures were laterally surrounded by an AlN shell,[48] and the whole structure was embedded in a rectangular prism of air, which permits elastic deformation. A schematic view of the structure excluding and including the AlN shell is presented in Figure 1a and b, respectively.

The 3D strain distribution was calculated by minimization of the elastic energy[48,49] through the application of zero-stress boundary conditions at the surface, which allowed the NW to deform in all three spatial directions. Figure 1a and b displays cross-sectional views of the strain components along the ⟨0001⟩ direction, e_{zz}, and along the <11−20> direction, e_{xx}, for a NW containing a 4 nm/4 nm GaN/AlN sequence, excluding and including a 5-nm-thick AlN shell, respectively. Figure 1c compares the e_{zz} profile in both cases. In the absence of a shell, the heterostructure evolves toward an equilibrium situation where the GaN NDs are compressively strained and the barriers are tensile strained. In the center of the NW, the relationship between $e_{zz} = -1.23\%$ and $e_{xx} = 0.66\%$ approaches the biaxial strain configuration ($e_{zz}/e_{xx} = -2c_{13}/c_{33} \approx 0.5327$, with the elastic constants $c_{13} = 106$ GPa and $c_{33} = 398$ GPa for GaN[50]). However, at the air−NW interface, the structure is almost fully relaxed. The presence of an AlN shell results in the application of a uniaxial compressive stress along ⟨0001⟩. As a result, in the center of the NDs, $e_{xx} = -1.28\%$ is still dominated by the pseudomorphic axial heterostructures, but the deformation along the growth axis is reduced to $e_{zz} = 0.006\%$.

For the calculation of the band profiles the spontaneous polarization and the piezoelectric fields resulting from the strain distribution were taken into account. The effect of surface states was simulated by introducing a two-dimensional (2D) charge density at the air/NW interface. We considered a surface charge of $\sigma = -2 \times 10^{12}$ cm^{-2}, which is a low value for a chemically clean GaN *m*-surface according to the measurements of Bertelli et al.[51] Figure 2a displays the conduction band profile at the center of the NW, comparing the cases of a NW heterostructure including and excluding the AlN shell, with and without surface states. The presence of surface charges fully depletes the GaN NW base, in agreement with previous studies and calculations.[47,52−54] The difference between the GaN polarization and the average polarization of the GaN/AlN heterostructure results in the formation of a depletion region at the base/heterostructure interface and an accumulation region at the heterostructure/cap layer interface. The GaN/AlN sequence presents the sawtooth profile characteristic of GaN/AlN superlattices, due to the spontaneous and piezoelectric polarization differences between GaN and AlN. The effect of surface charges in the heterostructure region is negligible; that is, the density of surface states considered is not enough to screen the polarization effect. Given the N polarity of the NW, the internal electric field in the NDs shifts the conduction band ground state toward the base of the NW, whereas the valence band ground state is shifted toward the top of the NW. The magnitude of the electric field is not significantly affected by the presence of the AlN shell, and it remains at 4.7 ± 0.1 MV/cm for all of the NDs, identical to the value expected for GaN/AlN (4 nm/4 nm) QWs. This is due to the fact that the change in

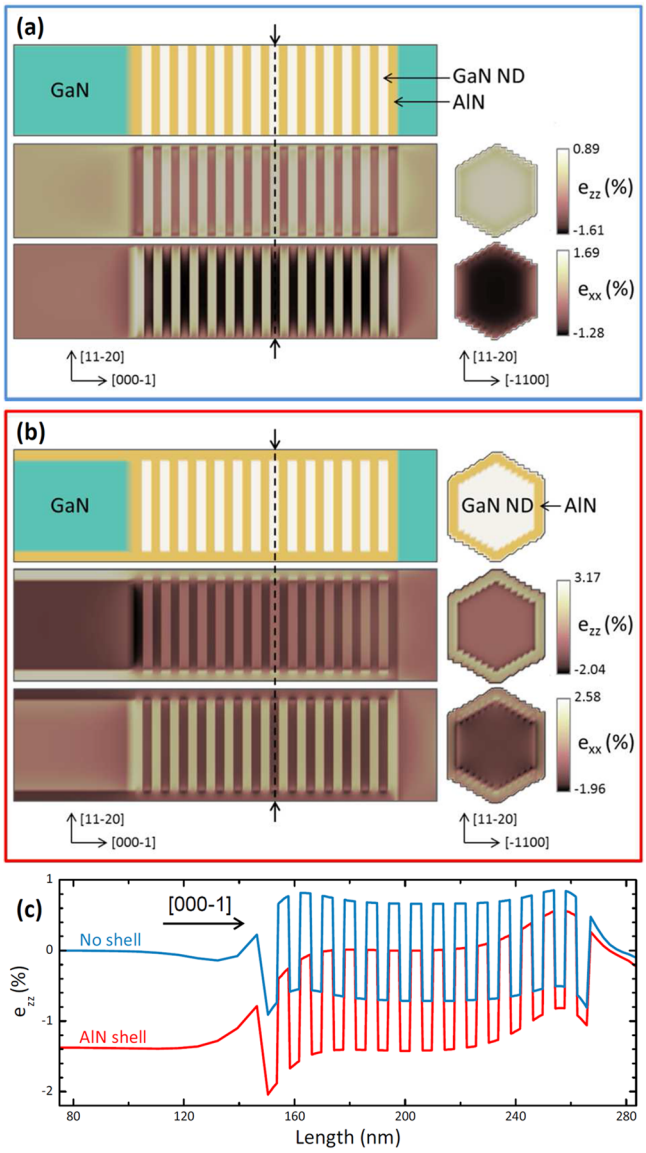

Figure 1. (a) From top to bottom, schematic material description of the simulated structure and cross-sectional views of the e_{zz} and e_{xx} strain components for a NW without AlN shell. The simulated NW incorporates 14 GaN/AlN (4 nm/4 nm) sections, and it has a radius of 20 nm in the <11−20> direction. Left: cross-sectional view along [1−100] at the center or the NW. Right: cross-sectional view along [0001] taken at the center of the eighth GaN ND (vertical dashed line on the left). (b) The same for a nanowire with a 5-nm-thick AlN shell as indicated in the schematic material description. (c) Comparison of the e_{zz} profile at along ⟨0001⟩ down the center of the NW, for a structure without shell and one with a 5-nm-thick AlN shell.

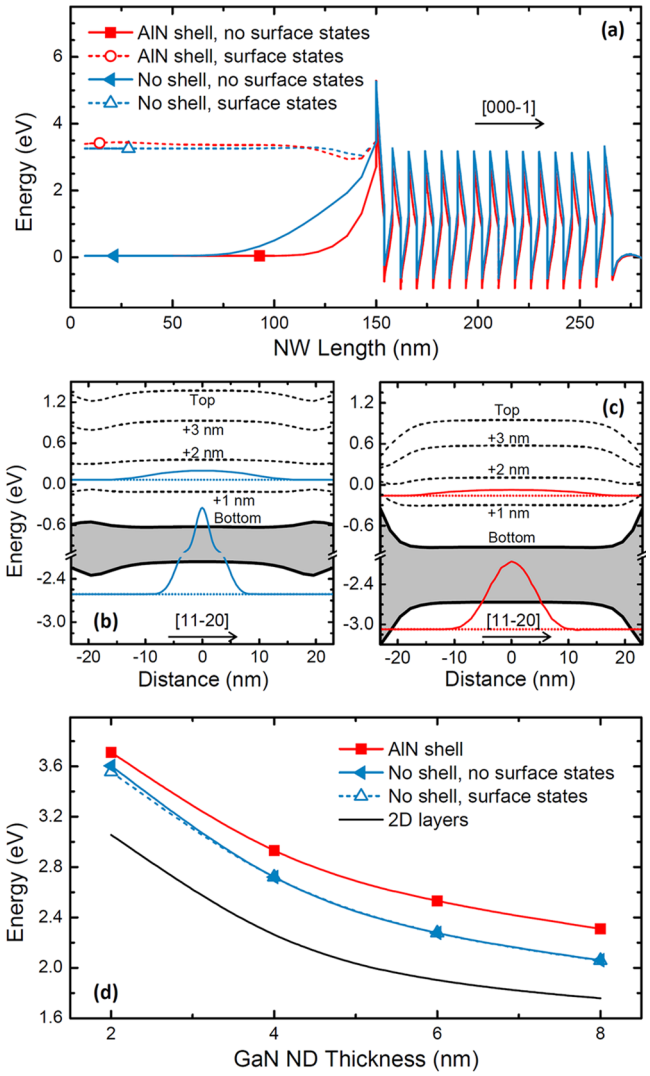

Figure 2. (a) Simulated conduction band profile along ⟨0001⟩ at the center of the NW for structures with and without shell, with and without surface states. Below, conduction (valence) band profiles obtained at the bottom (top) of the eighth GaN ND in (b) a NW without shell and (c) a NW with a 5-nm-thick AlN shell. A cross section of the probability density distribution, $|\Psi(\mathbf{r})|^2$ for the lower confined level in the conduction band and the higher confined level in the valence band is included. Dashed lines describe the variation of the conduction band profile when moving from the bottom to the top of the GaN ND; distances from the bottom of the ND are indicated. (d) Theoretical energy of the band-to-band transition energy as a function of the GaN ND thickness. Data are compared to the transition in the case of GaN/AlN QWs (2D layers).

piezoelectric polarization in the GaN NDs is compensated by the corresponding change in the AlN barriers.

The conduction (valence) band profiles along <11−20> obtained near the top (bottom) of a GaN ND are presented in Figure 2 for the cases of (b) a NW without shell and (c) a NW with a 5-nm-thick AlN shell. Results with and without surface states are indistinguishable in both cases. Cross sections of the squared wave functions, $|\Psi(\mathbf{r})|^2$ for the lower confined level in the conduction band and the higher confined level in the valence band are included. Conduction band profiles were taken at different heights within the GaN ND. Starting from the bottom of the ND, and moving upward, the conduction band profile can be seen at different points throughout the ND, as illustrated with dashed lines. At the bottom of the ND, the potential minimum is located at the center of the NW, whereas at the top of the ND, the potential minimum is located near the surface or at the ND/AlN-shell interface, that is, when migrating from the bottom to the top of the ND, the conduction band profile seems to inflate in the center. The addition of the AlN shell induces band pinning at the ND/AlN-shell interface, in conjunction with an increased rate of conduction band inflation. This band profile evolution is a direct consequence of the radial strain distribution in the ND.

Figure 2d describes the evolution of the band-to-band transition in the ND as a function of the ND thickness,

dx.doi.org/10.1021/nl5002247 | Nano Lett. 2014, 14, 1665−1673

comparing NWs including and excluding the AlN shell to GaN/AlN QWs. The lateral confinement within the NW geometry induces a blue shift of the interband transition, which cannot be justified solely by a change in the strain distribution (as explained above, the center of the NW keeps the biaxial strain configuration and the relaxation is limited to the vicinity of the surface). In the presence of the AlN shell, the uniaxial compressive strain along ⟨0001⟩ results in an increase of the GaN band gap, which further blue shifts the band-to-band transition. This uniaxial strain component is fundamental to understanding the PL from GaN/Al(Ga)N heterostructured NWs.[32,48]

Figure 3a presents cross-sectional views of the square wave function, $|\Psi(\mathbf{r})|^2$, for the three lowest electron states (s, p_x, p_y) in a GaN/AlN (4 nm/4 nm) ND, and the first excited states with secondary nodes along the growth axis (p_z, $p_{z,x}$, $p_{z,y}$). The data corresponds to a NW with a 5-nm-thick AlN shell, but it is qualitatively similar for NWs without a shell. As a result of the polarization-induced internal electric field, the lower electron state (s) is shifted toward the bottom of ND (maximum probability density ∼0.7 nm above the bottom of the ND). In contrast, the first excited state with a secondary node along the growth axis (p_z) presents a ring-shaped maximum probability density spatially located at the vertical center of the ND (∼2.0 nm from the bottom of the ND). This difference in location means that the wave function is distorted by the potential distribution in the center of the ND, presented in Figure 2b and c, where the potential minimum is located near the ND/AlN-shell interface, as opposed to in the center. Therefore, the s and p_z wave functions are not only vertically shifted due to the polarization-induced electric field, but also laterally due to the radial strain distribution in the ND. This lateral shift does not appear in the case of GaN/AlN QDs, where the hydrostatic compressive strain radially confines all the ground-state and excited electrons, as well as holes toward the center of the QD.[55,56] In comparison to QWs/QDs, the ND's lack of spatial overlap between the excited and ground electronic states results in a reduced oscillator strength, which should translate into slower (and nonexponential) intraband carrier relaxation, with a high dependence on the NW radius.

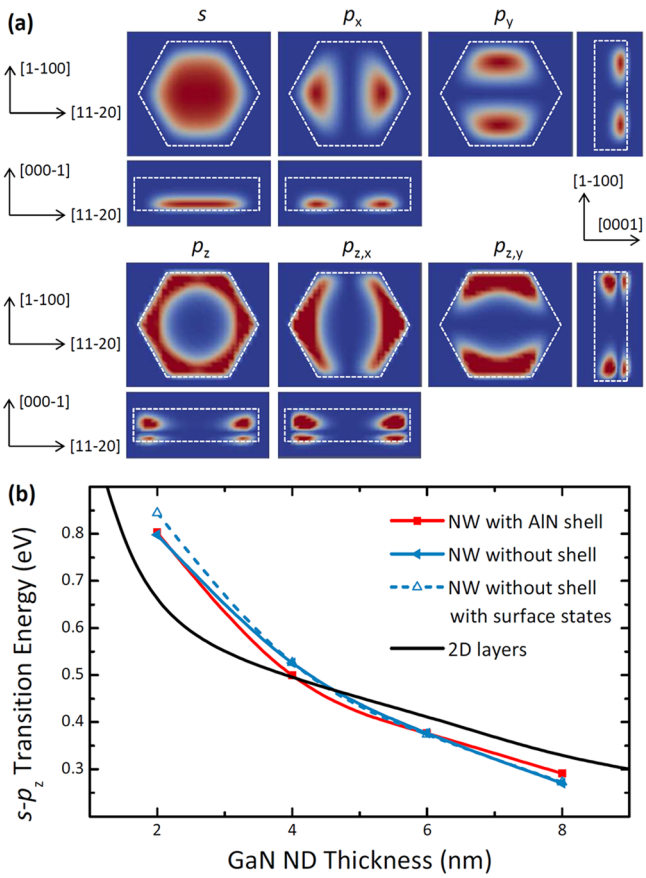

Figure 3. (a) Probability density distribution, $|\Psi(\mathbf{r})|^2$, for the three lowest electron states (s, p_x, p_y) in a GaN/AlN (4 nm/4 nm) ND in a NW with a radius of 20 nm (data correspond to a NW with a 5-nm-thick AlN shell). Below, first excited states due to confinement along the growth axis (p_z, $p_{z,x}$, $p_{z,y}$). The energies of the electron states with respect to the conduction band ground state, s, are calculated to be E_{px} = 27.6 meV, E_{py} = 28.8 meV, E_{pz} = 496 meV, E_{pzx} = 496 meV, E_{pzy} = 496 meV. (b) Variation of the s−p_z transition as a function of the GaN ND thickness in the case of a NW with an AlN shell, without shell without surface states, and without shell with a surface charge $\sigma = -2 \times 10^{12}$ cm^{-2}. Data are compared to the e_2−e_1 energy difference in the case of GaN/AlN QWs, calculated following ref 44.

It is important to note that the shape of the wave functions depends on the geometry of the NDs. Current calculations are performed assuming that the NDs are hexagonal prisms. In the case of a ND stack where the radii of the disks decrease from top to bottom, the asymmetric strain distribution along ⟨0001⟩ results in a modified lateral potential profile, which shifts the conduction band potential minima toward the ND/AlN-shell interface even at the bottom of the NDs.[48] This reshapes the *s* wave function and generates a local $|\Psi(\mathbf{r})|^2$ minimum at the center of the NW and renders the wave function more ring-like.

Figure 3b displays the evolution of the s−p_z intraband transition as a function of the ND thickness, comparing various NW configurations with the e_1−e_2 transition in GaN/AlN (4 nm/4 nm) QWs. In this calculation it is assumed that the in-plane lattice parameter of the QW superlattice evolves to the minimum energy configuration, as has been experimentally observed.[57] The effect of the AlN shell is smaller for intraband transitions (∼50 meV) than for interband transitions (∼300 meV). This intraband energy shift is also smaller than the typical intraband absorption line width in GaN/AlN QWs or QDs (50−100 meV[24]).

To study the influence of the NW radius, calculations were performed for NWs containing GaN/AlN NDs with 4-nm-thick AlN barriers and different ND thicknesses (2−8 nm) as well as different NW radii (14−26 nm). The interband and s−p_z intraband transition energies were calculated, and each showed changes of less than 4% over the investigated NW radial range. On the contrary, when analyzing the s−p_x or s−p_y transitions, the radius of the NW plays a large role in the discretization. Considering a ND of height 4 nm, the s−p_x or s−p_y transition occurs around 45 meV (∼27 μm) for a NW radius of 14 nm, versus 3 meV (∼410 μm) for a NW radius of 26 nm. This is attributed to the laterally confined states whose energy levels approach at higher NW radii.

Materials and Experimental Methods. N-polar GaN/AlN heterostructured NWs were grown catalyst-free by PAMBE on floating-zone Si(111) substrates in N-rich atmosphere (III/V ≈ 0.25) at ∼790 °C.[48] The NW vertical growth rate was 390 nm/h. They consist of a nonintentionally doped (n.i.d.) GaN base with a length of 600 nm and a radius of about 25−40 nm, followed by 40 periods of GaN/AlN sections, and a 20-nm-thick n.i.d. GaN cap layer. The thickness

dx.doi.org/10.1021/nl5002247 | Nano Lett. 2014, 14, 1665−1673

of the GaN sections (NDs) was varied between 3 and 8 nm, while the thickness of the AlN sections (barriers) was kept constant at 4 nm. The GaN NDs were doped with Ge, using a beam equivalent pressure (BEP_{Ge}) in the range of 0.5−1.5 × 10^{-9} mbar. Ge is known to dope *n*-type GaN NWs and to easily incorporate at large concentrations with weak impact on the NW morphology.[58] The structural details of the samples under study are summarized in Table 1.

Table 1. Description of the Samples under Study: GaN ND Thickness, BEP_{Ge} during the ND Growth, Low-Temperature (T = 5 K) PL Peak Wavelength, and Room-Temperature ISB Absorption Peak Wavelength

sample	ND thickness (nm)	BEP_{Ge} (mbar)	PL peak wavelength (nm)	ISB absorption peak wavelength (μm)
S1	4	0	454	
S2	4	5.0×10^{-10}	429	1.95
S3	4	1.0×10^{-9}	392	1.65
S4	4	1.5×10^{-9}	384	1.60
S5	3	9×10^{-10}	363	1.58
S6	4	9×10^{-10}	390	1.62
S7	6	9×10^{-10}	410	1.74
S8	7	9×10^{-10}	419	1.75
S9	8	9×10^{-10}	438	1.75

Structural and morphological characterization of the heterostructures was performed by high-resolution transmission electron microscopy (HRTEM) and annular dark field (ADF) scanning transmission electron microscopy (STEM) using a FEI Tecnai F20 field emission gun microscope operated at 200 kV. For microscopy studies, the NWs were directly scratched from the substrate with a holey carbon TEM grid.

PL spectra were obtained by exciting with a continuous-wave frequency-doubled Ar laser (λ = 244 nm), with an excitation power around 50 μW focused on a spot with a diameter of ∼100 μm. The emission from the sample was collected by a Jobin Yvon HR460 monochromator equipped with a UV-enhanced charge-coupled device (CCD) camera. Intraband absorption was probed by Fourier transform infrared spectroscopy (FTIR) performed in a Bruker V70v spectrometer using a halogen lamp, a CaF_2 beam splitter, and an HgCdTe detector. The transmission was measured at room temperature, in vacuum, with the sample tilted at the Brewster angle. The transmission spectra for TE- and TM-polarized light are corrected by the corresponding transmission of a sample containing 1-μm-long n.i.d. GaN NWs on floating zone Si(111).

Results and Discussion. For a correct interpretation of the optical studies, the geometry and dimensions of the heterostructures have been analyzed by transmission electron microscopy methods. Figure 4 shows ADF and HRTEM images of samples S6 and S9, which confirm the growth of the wires along the ⟨0001⟩ direction for both phases, GaN and AlN, with a perfect epitaxy consecutively achieved between both materials. The GaN/AlN heterostructures are enveloped by a thin (2−5 nm) AlN layer, starting from the topmost AlN barrier extending along the GaN stem. Electron energy loss spectroscopy (EELS) measurements demonstrate that there is no interdiffusion of Ga or Al, confirming sharp interfaces between the NDs and the barriers.

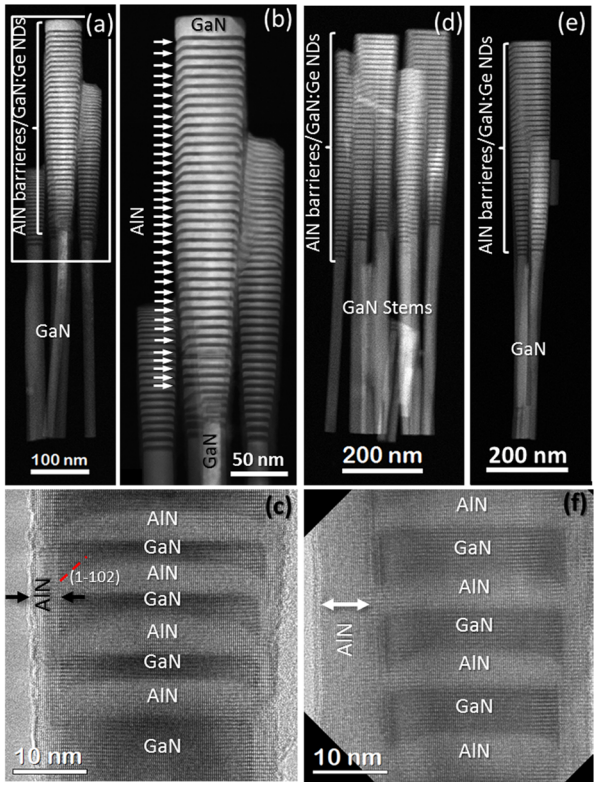

Figure 4. (a) ADF image of a set of GaN NWs from sample S6, containing 40 periods of AlN/GaN NDs. (b) Zoom-in of the squared area in (a). (c) HRTEM image of several GaN NDs and AlN barriers. (d,e) ADF images of sets of wires from sample S9. (f) HRTEM image of several GaN NDs, separated by AlN barriers.

In the HRTEM images, we observe that the AlN sections often present {1−102} facets close to the surface. To quantify the effect of this AlN {1−102} faceting on the electronic transitions, we have modeled NWs containing GaN/AlN heterostructures with a GaN ND thickness varying from 2 to 8 nm and with AlN barriers consisting of a hexagonal prism of 2 nm followed by a 2-nm-thick hexagonal truncated pyramid with {1−102} facets. Compared with the nonfaceted structures presented above, faceted structures have on average a 10% lower interband energy difference, as well as a 6% higher s−p_z intraband energy difference.

The measurement of intraband absorption requires the first electronic level of the nanostructures to be populated with electrons. Therefore, we analyzed a series of NWs containing a 40-period GaN:Ge/AlN (4 nm/4 nm) heterostructure with different Ge doping levels (samples S1−S4 in Table 1). According to time-of-flight secondary ion mass spectroscopy (ToF-SIMS) measurements,[58] the various BEP_{Ge} (5.0×10^{-10}, 1.0×10^{-9}, and 1.5×10^{-9} mbar) should produce Ge concentrations of [Ge] ∼ 9×10^{-19}, 1.7×10^{-20}, and 3.1×10^{-20} cm^{-3}, respectively. Figure 5 presents the results of (a) interband (PL) and (b) intraband (FTIR) optical characterization of this series. The low-temperature (T = 5 K) PL peak wavelength of the structures blue shifts more than 70 nm (see Table 1) and broadens for increasing doping levels, which can be assigned to the screening of the polarization-induced internal electric field in the NDs by the free carriers.[59] This further supported by the agreement between the experimental results and theoretical calculations for the band-to-band

dx.doi.org/10.1021/nl5002247 | *Nano Lett.* 2014, 14, 1665−1673

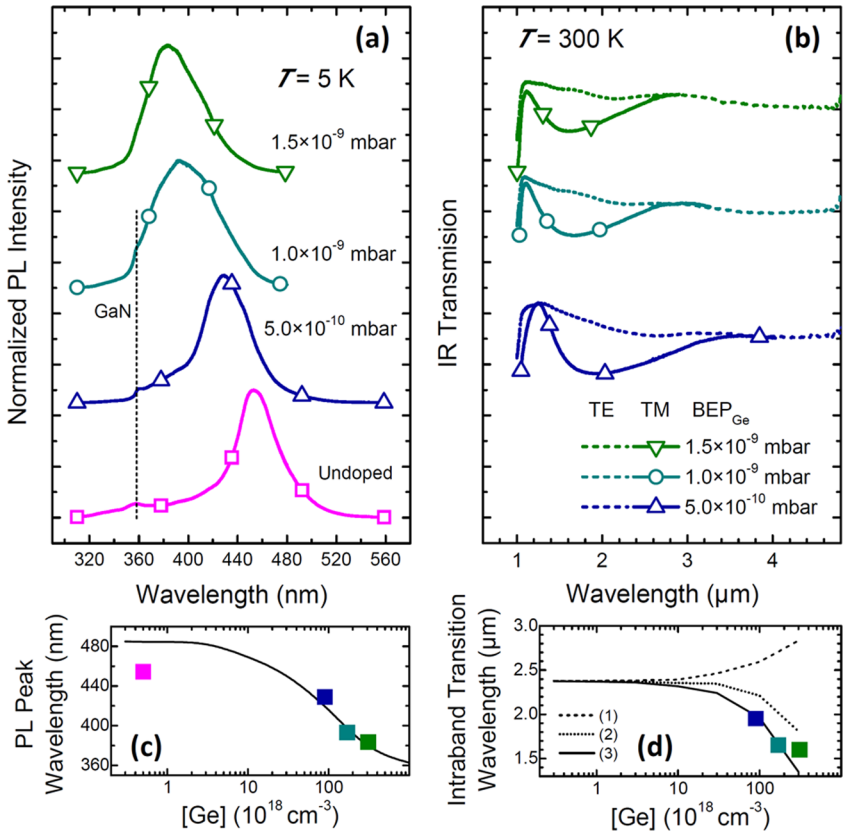

Figure 5. (a) Low-temperature PL spectra of Ge-doped GaN/AlN (4 nm/4 nm) heterostructured NWs with different doping levels in the GaN NDs (samples S1−S4 in Table 1). The spectra are normalized by their maximum and vertically shifted for clarity. The BEP_{Ge} used for Ge doping is indicated by each curve. The emission wavelength of the GaN base is indicated by a vertical dashed line. (b) Room-temperature IR transmission spectra for TE-(dashed) and TM-polarized (solid) light measured for Ge-doped GaN/AlN (4 nm/4 nm) heterostructured NWs with different doping levels in the GaN NDs. The spectra are vertically shifted for clarity. (c) Variation of the PL peak wavelength as a function of the estimated Ge concentration. Dots are experimental values from (a); the solid line is a theoretical calculation of the band-to-band transition at low temperature using a 3D model of the structure. (d) Variation of the intraband transition wavelength as a function of the estimated Ge concentration. Dots are experimental values from (b); the dashed line labeled (1) is a 1D calculation of the intraband transition accounting for the screening of the internal electric field; the dotted line (2) incorporates corrections associated to both screening and exchange interaction; the solid line (3) accounts for screening, exchange interaction, and depolarization shift.

transitions using a 3D model and including the screened internal electric fields (see Figure 5c).[60]

The intraband absorption was investigated at room temperature by measuring the IR transmission of the samples in an FTIR system, with the results depicted in Figure 5b. The dip in the IR transmission for TM-polarized light is assigned to the s−p_z transition, following the intraband polarization selection rules. This intraband absorption line shifts systematically toward shorter wavelengths with increasing dopant concentration, in contradiction to simulations considering only the screening of the polarization-induced internal electric field.[35] This discrepancy between simulations and experiments is attributed to many-body effects. We have previously shown the relevance of these many-body phenomena in the case of GaN/Al(Ga)N QWs,[61,62] where their magnitudes can be comparable to the value of the e_2−e_1 transition energy.[63]

To explain the experimental results, two kinds of many-body effects must be considered, namely, those modifying the energy levels (exchange interaction) and those modifying the intraband absorption energy (plasmon screening and excitonic shift).[64] The exchange interaction is due to the repulsion between electrons with the same spin, following the Pauli exclusion principle. We have estimated the shift induced by the exchange interaction, E_{exch}, following a one-dimensional (1D) approach, using the Hartree−Fock method with the approximation by Bandara et al.[65,66]

$$E_{exch}(k) = \frac{-e^2 k_F}{4\pi\varepsilon\varepsilon_0}\left[\frac{2}{\pi}\mathbf{E}(k/k_F) - 0.32(k_F/k_L)\right] \quad (1)$$

where e is the electron charge, ε the dielectric constant, ε_0 the vacuum permittivity, $k_F = (2\pi n_S)^{1/2}$ with n_S being the surface charge density *in* the well, $k_L = \pi/L$ with L being the QW thickness, and $\mathbf{E}(k/k_F)$ is a complete elliptical integral of the second kind.

The shift of the intraband absorption energy induced by plasmon screening (depolarization shift) and by the Coulomb interaction between the excited electron and the quasi-hole left in the ground state (excitonic or final-state interaction), was calculated as[64]

$$E_{12} = (e_2 - e_1)\sqrt{1 + \alpha - \beta} \quad (2)$$

where e_1 and e_2 are the energies of the first and second electronic levels in the well, and α and β (both >0) represent the depolarization shift and the exciton interaction, respectively. The frequency shift α was calculated by numerical methods following[64,67]

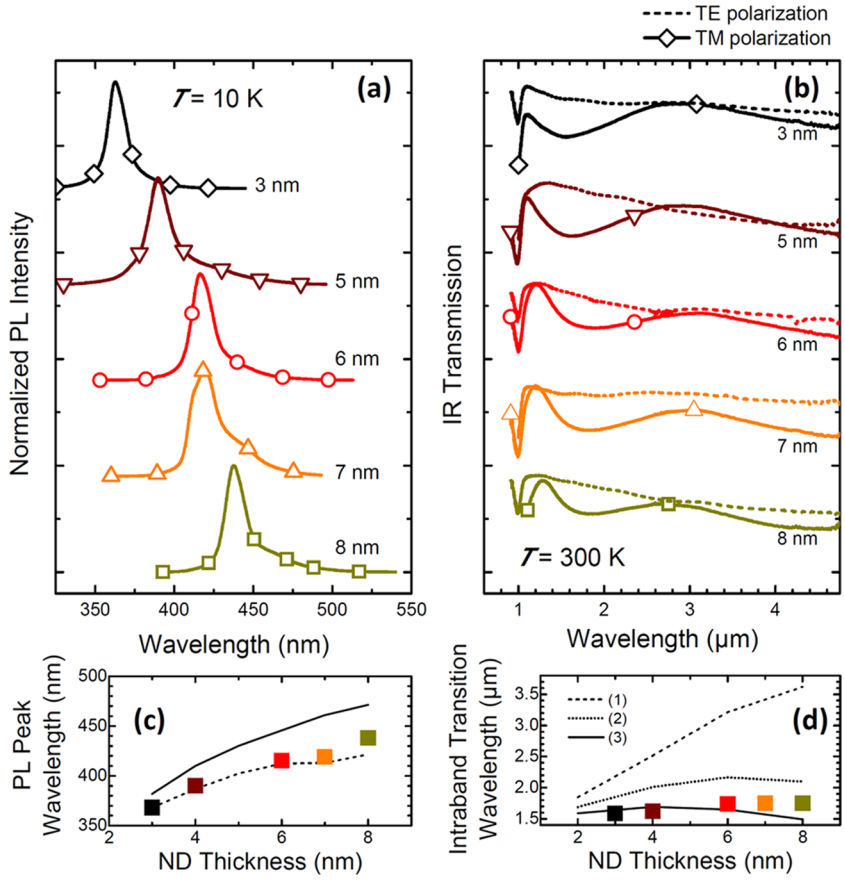

Figure 6. (a) Low-temperature PL spectra of Ge-doped GaN/AlN heterostructured NWs with 4-nm-thick AlN barriers and various GaN ND thicknesses as indicated (samples S5−S9 in Table 1). The spectra are normalized by their maximum and vertically shifted for clarity. (b) Room-temperature IR transmission spectra for TE- and TM-polarized light measured for Ge-doped GaN/AlN heterostructured NWs with different GaN ND thickness. The spectra are vertically shifted for clarity. (c) Variation of the PL peak wavelength as a function of the ND thickness. Dots are experimental values from (a); the solid line is a theoretical calculation of the band-to-band transition at low temperature using a 3D model of the structure and assuming [Ge] = 1.5×10^{20} cm^{-3}; the dashed line assumes [Ge] = 2.4×10^{20} cm^{-3}. (d) Variation of the intraband transition wavelength as a function of the ND thickness. Dots are experimental values from (b); the dashed line labeled (1) is a 1D calculation of the intraband transition accounting for the screening of the internal electric field; the dotted line (2) incorporates corrections associated to both screening and exchange interaction; the solid line (3) accounts for screening, exchange interaction, and depolarization shift.

$$\alpha = \frac{2e^2 n_S}{\varepsilon\varepsilon_0(e_2 - e_1)} \int_{-\infty}^{\infty} dz \left[\int_{-\infty}^{z} \Psi_2(z')\Psi_1(z')\, dz'\right]^2 \quad (3)$$

with $\Psi_1(z')$ and $\Psi_2(z')$ being the wave functions associated to e_1 and e_2, respectively. The values of $\Psi_1(z')$, $\Psi_2(z')$, e_1, and e_2 were extracted using the Nextnano3 Schrödinger−Poisson equation solver. The values of β (after eq 59 in ref 64) were found to be at least 2 orders of magnitude smaller than α (as it is also in the case of GaAs QWs) and were therefore neglected in the calculations.

Figure 5d depicts the predicted red shift of e_2−e_1 with increasing doping level, based on the Nextnano3 calculations taking the screening of the internal electric field into account (dashed line). Introducing the corrections associated to the exchange interaction (eq 1) and depolarization shift (eqs 2 and 3) translates into a blue shift of the absorption which can reach several hundreds of nanometers (solid line). The theoretical results are in good agreement with the experimental data, assuming fully ionized Ge dopants, with a density that is estimated from the BEP_{Ge} and compared to ToF-SIMS measurements in ref 58.

The s−p_x and s−p_y transitions, predicted in the far-IR around 40−50 μm and sensitive to TE-polarization, were not experimentally observed. This might be explained, by the dispersion introduced by the fluctuations in the NW radius, or by the fact that the NW geometry is expected to preferentially interact with TM coupled light and hence hinder the absorption of TE-polarized light.[54,68]

In conjunction to these experiments, we have analyzed a series of NWs containing 40-period GaN:Ge/AlN heterostructures with 4-nm-thick AlN barriers and various GaN ND thicknesses (samples S5−S9 in Table 1), all of them were doped with Ge using $BEP_{Ge} = 9 \times 10^{-10}$ mbar (estimated [Ge] ~ 1.5×10^{20} cm^{-3}). The low-temperature (T = 5 K) PL peak energy from these samples, presented in Figure 6a, blue shifts for increasing ND thickness. This evolution is qualitatively described by theoretical calculations of the band-to-band transition using a 3D model which takes the screening of the internal electric field into account (see Figure 6c).[69] The blue shift of the experimental data with respect to the model could be explained by an underestimation of the effective dopant concentration (note the good agreement with the dashed-line calculations, which assume [Ge] ~ 2.4×10^{20} cm^{-3}).

Room-temperature IR transmission measurements of this series are summarized in Figure 5b. As described above, the dip in the IR transmission for TM-polarized light is assigned to the

dx.doi.org/10.1021/nl5002247 | Nano Lett. 2014, 14, 1665−1673

s−p_z transition, which shifts systematically toward longer wavelengths for thicker NDs. Figure 6d compares the experimental data to predictions made by Nextnano3 taking the screening of the internal electric field into account (dashed line). Introducing the corrections associated to the exchange interaction (eq 1) and depolarization shift (eqs 2 and 3) translates into a blue-shifted transition, which fits the experimental absorption data.

Limitations. It is important to keep in mind the limitations associated with the calculations of many-body effects. The models of the exchange interaction and the depolarization shift described above are approximations that consider these effects as a perturbation of the Hartree−Fock equation.[64] Equation 1 is an approximation that accounts for the deformation of the ground state assuming square QWs,[65,66] and eq 3 is extracted from a two-level model which requires that there is significant oscillator strength for transitions to only one excited state.[67] Looking at the order of magnitude of the experimental spectral shifts, comparable to the e_2-e_1 energy, the validity of these approximations is arguable. They provide a valid qualitative description, but a rigorous solution of the Hartree−Fock equation would be required, which is beyond the scope of this work.

Conclusions. From the theoretical analysis of the band diagram and electronic structure of GaN NWs containing a sequence of GaN/AlN NDs, we conclude that the formation of an AlN shell during the heterostructure growth results in a uniaxial compressive strain that blue shifts the interband optical transitions but does not have a critical influence on the intraband transitions. The presence of surface states with the density levels expected for the *m*-GaN plane causes a charge depletion of the base of the NWs, but it is not high enough to screen the polarization-induced internal electric field in the heterostructures. Variations in the NW radius do not modify significantly the interband or s−p_z intraband transitions, but they shift the intraband levels associated to the lateral confinement (p_x, p_y).

From the experimental viewpoint, we report the observation of a TM-polarized IR absorption line assigned to the s−p_z intraband transition in Ge-doped GaN/AlN NDs inserted in self-assembled GaN NWs grown on Si(111) by PAMBE. The s−p_x and s−p_y intraband transitions are not observed, most likely due to fluctuations of the NW radius and to the preferential coupling of TM light to the NW geometry. For increasing doping levels, we observe a broadening and blue shift of the PL as a result of the screening of the polarization-induced internal electric field in the NDs. Regarding intraband transitions, doping induces a blue shift of the s−p_z absorption line attributed to many-body effects, namely, the exchange interaction and depolarization shift, which dominate the red shift induced by internal electric field screening. The s−p_z transition red shifts with increasing ND thickness as theoretically expected.

AUTHOR INFORMATION

Notes

The authors declare no competing financial interest.

ACKNOWLEDGMENTS

This work was partially supported by the EU ERC-StG "TeraGaN" (#278428) project. M.d.l.M. thanks CSIC JAE-Predoc program. J.A. acknowledges the funding from the Spanish MICINN project MAT2010-15138 (COPEON) and Generalitat de Catalunya (2009 SGR770). The authors thank the TEM facilities at ICN2 (BNC-b, UAB).

REFERENCES

(1) Moumanis, K.; Helman, A.; Fossard, F.; Tchernycheva, M.; Lusson, A.; Julien, F. H.; Damilano, B.; Grandjean, N.; Massies, J. *Appl. Phys. Lett.* **2003**, *82*, 868−870.
(2) Tchernycheva, M.; Nevou, L.; Doyennette, L.; Helman, A.; Colombelli, R.; Julien, F. H.; Guillot, F.; Monroy, E.; Shibata, T.; Tanaka, M. *Appl. Phys. Lett.* **2005**, *87*, 101912.
(3) Guillot, F.; Bellet-Amalric, E.; Monroy, E.; Tchernycheva, M.; Nevou, L.; Doyennette, L.; Julien, F. H.; Dang, L. S.; Remmele, T.; Albrecht, M.; Shibata, T.; Tanaka, M. *J. Appl. Phys.* **2006**, *100*, 044326.
(4) Vardi, A.; Bahir, G.; Schacham, S. E.; Kandaswamy, P. K.; Monroy, E. *Phys. Rev. B* **2009**, *80*, 155439.
(5) Chia-Fu, H.; Jeong-Seok, O.; Zory, P.; Botez, D. *IEEE J. Sel. Top. Quantum Electron.* **2000**, *6*, 491−503.
(6) Zibik, E. A.; Grange, T.; Carpenter, B. A.; Porter, N. E.; Ferreira, R.; Bastard, G.; Stehr, D.; Winnerl, S.; Helm, M.; Liu, H. Y.; Skolnick, M. S.; Wilson, L. R. *Nat. Mater.* **2009**, *8*, 803−807.
(7) Krall, M.; Brandstetter, M.; Deutsch, C.; Detz, H.; Zederbauer, T.; Andrews, A. M.; Schrenk, W.; Strasser, G.; Unterrainer, K.; Belyanin, A. A.; Smowton, P. M. *Proc. SPIE* **2013**, *8640*, 864018−864018-7.
(8) Grange, T. *arXiv:1301.1258* **2013**.
(9) Lu, W.; Lieber, C. M. *Nat. Mater.* **2007**, *6*, 841−850.
(10) Deshpande, S.; Heo, J.; Das, A.; Bhattacharya, P. *Nat. Commun.* **2013**, *4*, 1675.
(11) Nakayama, Y.; Pauzauskie, P. J.; Radenovic, A.; Onorato, R. M.; Saykally, R. J.; Liphardt, J.; Yang, P. *Nature* **2007**, *447*, 1098−1101.
(12) Wu, W.; Wen, X.; Wang, Z. L. *Science* **2013**, *340*, 952−957.
(13) Wallentin, J.; Anttu, N.; Asoli, D.; Huffman, M.; Aberg, I.; Magnusson, M. H.; Siefer, G.; Fuss-Kailuweit, P.; Dimroth, F.; Witzigmann, B.; Xu, H. Q.; Samuelson, L.; Deppert, K.; Borgstrom, M. T. *Science* **2013**, *339*, 1057−1060.
(14) Cui, Y. *Science* **2001**, *293*, 1289−1292.
(15) Wallys, J.; Teubert, J.; Furtmayr, F.; Hofmann, D. M.; Eickhoff, M. *Nano Lett.* **2012**, *12*, 6180−6186.
(16) Black, M.; Lin, Y.-M.; Cronin, S.; Rabin, O.; Dresselhaus, M. *Phys. Rev. B* **2002**, *65*, 195417.
(17) Rustagi, S. C.; Singh, N.; Lim, Y. F.; Zhang, G.; Wang, S.; Lo, G. Q.; Balasubramanian, N.; Kwong, D.-L. *IEEE Electron Device Lett.* **2007**, *28*, 909−912.
(18) Dubrovskii, V. G.; Sibirev, N. V. *Phys. Rev. B* **2008**, *77*, 035414.
(19) Akiyama, T.; Yamashita, T.; Nakamura, K.; Ito, T. *Nano Lett.* **2010**, *10*, 4614−4618.
(20) Thelander, C.; Caroff, P.; Plissard, S.; Dey, A. W.; Dick, K. A. *Nano Lett.* **2011**, *11*, 2424−2429.
(21) Amanti, M. I.; Bismuto, A.; Beck, M.; Isa, L.; Kumar, K.; Reimhult, E.; Faist, J. *Opt. Express* **2013**, *21*, 10917.
(22) Hofstetter, D.; Baumann, E.; Giorgetta, F. R.; Théron, R.; Wu, H.; Schaff, W. J.; Dawlaty, J.; George, P. A.; Eastman, L. F.; Rana, F.; Kandaswamy, P. K.; Guillot, F.; Monroy, E. *Proc. IEEE* **2010**, *98*, 1234−1248.
(23) Machhadani, H.; Kandaswamy, P.; Sakr, S.; Vardi, A.; Wirtmüller, A.; Nevou, L.; Guillot, F.; Pozzovivo, G.; Tchernycheva, M.; Lupu, A.; Vivien, L.; Crozat, P.; Warde, E.; Bougerol, C.; Schacham, S.; Strasser, G.; Bahir, G.; Monroy, E.; Julien, F. H. *New J. Phys.* **2009**, *11*, 125023.
(24) Beeler, M.; Trichas, E.; Monroy, E. *Semicond. Sci. Technol.* **2013**, *28*, 074022.
(25) Binggeli, N.; Ferrara, P.; Baldereschi, A. *Phys. Rev. B* **2001**, *63*, 245306.
(26) Cociorva, D.; Aulbur, W. G.; Wilkins, J. W. *Solid State Commun.* **2002**, *124*, 63−66.
(27) Tchernycheva, M.; Nevou, L.; Doyennette, L.; Julien, F.; Warde, E.; Guillot, F.; Monroy, E.; Bellet-Amalric, E.; Remmele, T.; Albrecht, M. *Phys. Rev. B* **2006**, *73*, 125347.

(28) Iizuka, N.; Kaneko, K.; Suzuki, N.; Asano, T.; Noda, S.; Wada, O. *Appl. Phys. Lett.* **2000**, *77*, 648−650.
(29) Heber, J. D.; Gmachl, C.; Ng, H. M.; Cho, A. Y. *Appl. Phys. Lett.* **2002**, *81*, 1237−1239.
(30) Iizuka, N.; Kaneko, K.; Suzuki, N. *Opt. Express* **2005**, *13*, 3835−3840.
(31) Hamazaki, J.; Kunugita, H.; Ema, K.; Kikuchi, A.; Kishino, K. *Phys. Rev. B* **2005**, *71*, 165334.
(32) Songmuang, R.; Katsaros, G.; Monroy, E.; Spathis, P.; Bougerol, C.; Mongillo, M.; De Franceschi, S. *Nano Lett.* **2010**, *10*, 3545−3550.
(33) Rigutti, L.; Jacopin, G.; Bugallo, A. D. L.; Tchernycheva, M.; Warde, E.; Julien, F. H.; Songmuang, R.; Galopin, E.; Largeau, L.; Harmand, J.-C. *Nanotechnology* **2010**, *21*, 425206.
(34) Suzuki, N.; Iizuka, N. *Jpn. J. Appl. Phys.* **1999**, *38*, L363−L365.
(35) Kandaswamy, P. K.; Machhadani, H.; Bougerol, C.; Sakr, S.; Tchernycheva, M.; Julien, F. H.; Monroy, E. *Appl. Phys. Lett.* **2009**, *95*, 141911.
(36) Péré-Laperne, N.; Bayram, C.; Nguyen-The, L.; McClintock, R.; Razeghi, M. *Appl. Phys. Lett.* **2009**, *95*, 131109.
(37) Bayram, C. *J. Appl. Phys.* **2012**, *111*, 013514.
(38) Edmunds, C.; Tang, L.; Shao, J.; Li, D.; Cervantes, M.; Gardner, G.; Zakharov, D. N.; Manfra, M. J.; Malis, O. *Appl. Phys. Lett.* **2012**, *101*, 102104.
(39) Tian, W.; Yan, W. Y.; Hui, X.; Li, S. L.; Ding, Y. Y.; Li, Y.; Tian, Y.; Dai, J. N.; Fang, Y. Y.; Wu, Z. H.; Yu, C. H.; Chen, C. Q. *J. Appl. Phys.* **2012**, *112*, 063526.
(40) Machhadani, H.; Kotsar, Y.; Sakr, S.; Tchernycheva, M.; Colombelli, R.; Mangeney, J.; Bellet-Amalric, E.; Sarigiannidou, E.; Monroy, E.; Julien, F. H. *Appl. Phys. Lett.* **2010**, *97*, 191101.
(41) Sudradjat, F. F.; Zhang, W.; Woodward, J.; Durmaz, H.; Moustakas, T. D.; Paiella, R. *Appl. Phys. Lett.* **2012**, *100*, 241113.
(42) Beeler, M.; Bougerol, C.; Bellet-Amalric, E.; Monroy, E. *Appl. Phys. Lett.* **2013**, *103*, 091108.
(43) Tanaka, K.; Ikuno, K.; Kasai, Y.; Fukunaga, K.; Kunugita, H.; Ema, K.; Kikuchi, A.; Kishino, K. *J. Lumin.* **2008**, *128*, 1084−1086.
(44) Birner, S.; Zibold, T.; Andlauer, T.; Kubis, T.; Sabathil, M.; Trellakis, A.; Vogl, P. *IEEE Trans. Electron Devices* **2007**, *54*, 2137−2142.
(45) Kandaswamy, P. K.; Guillot, F.; Bellet-Amalric, E.; Monroy, E.; Nevou, L.; Tchernycheva, M.; Michon, A.; Julien, F. H.; Baumann, E.; Giorgetta, F. R.; Hofstetter, D.; Remmele, T.; Albrecht, M.; Birner, S.; Dang, L. S. *J. Appl. Phys.* **2008**, *104*, 093501.
(46) De la Mata, M.; Magen, C.; Gazquez, J.; Utama, M. I. B.; Heiss, M.; Lopatin, S.; Furtmayr, F.; Fernández-Rojas, C. J.; Peng, B.; Morante, J. R.; Rurali, R.; Eickhoff, M.; Fontcuberta i Morral, A.; Xiong, Q.; Arbiol, J. *Nano Lett.* **2012**, *12*, 2579−2586.
(47) Den Hertog, M. I.; González-Posada, F.; Songmuang, R.; Rouviere, J. L.; Fournier, T.; Fernandez, B.; Monroy, E. *Nano Lett.* **2012**, *12*, 5691−5696.
(48) Furtmayr, F.; Teubert, J.; Becker, P.; Conesa-Boj, S.; Morante, J. R.; Chernikov, A.; Schäfer, S.; Chatterjee, S.; Arbiol, J.; Eickhoff, M. *Phys. Rev. B* **2011**, *84*, 205303.
(49) Rivera, C.; Jahn, U.; Flissikowski, T.; Pau, J.; Muñoz, E.; Grahn, H. T. *Phys. Rev. B* **2007**, *75*, 045316.
(50) Polian, A.; Grimsditch, M.; Grzegory, I. *J. Appl. Phys.* **1996**, *79*, 3343−3344.
(51) Bertelli, M.; Löptien, P.; Wenderoth, M.; Rizzi, A.; Ulbrich, R.; Righi, M.; Ferretti, A.; Martin-Samos, L.; Bertoni, C.; Catellani, A. *Phys. Rev. B* **2009**, *80*, 115324.
(52) Dobrokhotov, V.; McIlroy, D. N.; Norton, M. G.; Abuzir, A.; Yeh, W. J.; Stevenson, I.; Pouy, R.; Bochenek, J.; Cartwright, M.; Wang, L.; Dawson, J.; Beaux, M.; Berven, C. *J. Appl. Phys.* **2006**, *99*, 104302.
(53) Sanford, N. A.; Blanchard, P. T.; Bertness, K. A.; Mansfield, L.; Schlager, J. B.; Sanders, A. W.; Roshko, A.; Burton, B. B.; George, S. M. *J. Appl. Phys.* **2010**, *107*, 034318.
(54) González-Posada, F.; Songmuang, R.; Den Hertog, M.; Monroy, E. *Nano Lett.* **2012**, *12*, 172−176.
(55) Andreev, A.; O'Reilly, E. *Phys. Rev. B* **2000**, *62*, 15851−15870.
(56) Ranjan, V.; Allan, G.; Priester, C.; Delerue, C. *Phys. Rev. B* **2003**, *68*, 115303.
(57) Kandaswamy, P. K.; Bougerol, C.; Jalabert, D.; Ruterana, P.; Monroy, E. *J. Appl. Phys.* **2009**, *106*, 013526.
(58) Schörmann, J.; Hille, P.; Schäfer, M.; Müßener, J.; Becker, P.; Klar, P. J.; Kleine-Boymann, M.; Rohnke, M.; de la Mata, M.; Arbiol, J.; Hofmann, D. M.; Teubert, J.; Eickhoff, M. *J. Appl. Phys.* **2013**, *114*, 103505.
(59) Hille, P.; Müßener, J.; Becker, P.; de la Mata, M.; Rosemann, N.; Magén, C.; Arbiol, J.; Teubert, J.; Chatterjee, S.; Schörmann, J.; Eickhoff, M. *arXiv:1402.3081*, **2014**.
(60) The calculations used the same 3D model as the one described in Figure 1b and tried to approach the real structure using geometrical feedback from TEM images. The GaN base radius was 20 nm, the AlN shell thickness was 2 nm, the thickness of the GaN:Ge NDs was 3.7 nm, and the AlN barriers consisted of a hexagonal prism of 2 nm followed by a 2-nm-thick hexagonal truncated pyramid with {1−102} facets. Surface charges were neglected.
(61) Helman, A.; Tchernycheva, M.; Lusson, A.; Warde, E.; Julien, F. H.; Moumanis, K.; Fishman, G.; Monroy, E.; Daudin, B.; Le Si Dang, D.; Bellet-Amalric, E.; Jalabert, D. *Appl. Phys. Lett.* **2003**, *83*, 5196−5198.
(62) Kotsar, Y.; Doisneau, B.; Bellet-Amalric, E.; Das, A.; Sarigiannidou, E.; Monroy, E. *J. Appl. Phys.* **2011**, *110*, 033501.
(63) Kandaswamy, P. K.; Machhadani, H.; Kotsar, Y.; Sakr, S.; Das, A.; Tchernycheva, M.; Rapenne, L.; Sarigiannidou, E.; Julien, F. H.; Monroy, E. *Appl. Phys. Lett.* **2010**, *96*, 141903.
(64) Helm, M. In *Intersubband Transitions in Quantum Wells: Physics and Device Applications I*; Liu, H. C., Capasso, F., Eds.; Academic Press: San Diego, 2000.
(65) Bandara, K. M. S. V.; Coon, D. D.; O, B.; Lin, Y. F.; Francombe, M. H. *Appl. Phys. Lett.* **1988**, *53*, 1931.
(66) Bandara, K. M. S. V.; Coon, D. D.; O, B.; Lin, Y. F.; Francombe, M. H. *Appl. Phys. Lett.* **1989**, *55*, 206.
(67) Allen, S. J.; Tsui, D. C.; Vinter, B. *Solid State Commun.* **1976**, *20*, 425−428.
(68) Wang, J.; Gudiksen, M. S.; Duan, X.; Cui, Y.; Lieber, C. M. *Science* **2001**, *293*, 1455−1457.
(69) Note: The calculations used the same 3D model as the one described in Figure 1b. The GaN base radius was 20 nm, the AlN shell thickness was 2 nm, and the AlN barriers consisted of a hexagonal prism of 2 nm followed by a 2-nm-thick hexagonal truncated pyramid with {1−102} facets. Surface charges were considered to be $\sigma = -2 \times 10^{12}$ cm^{-2}.